

Van Hove singularity driven emergence of multiple flat band-like nondispersive features in kagome superconductors

Hailan Luo,^{1,2,*} Lin Zhao,^{1,2,3,*} Zhen Zhao,^{1,2,*} Haitao Yang,^{1,2,3,4,*} Yun-Peng Huang^①,¹ Hongxiong Liu,^{1,2} Yuhao Gu,¹ Feng Jin,¹ Hao Chen,^{1,2} Taimin Miao,^{1,2} Chaohui Yin,^{1,2} Chengmin Shen,¹ Xiaolin Ren,^{1,2} Bo Liang,^{1,2} Yingjie Shu,^{1,2} Yiwen Chen,^{1,2} Fengfeng Zhang,⁵ Feng Yang,⁵ Shenjin Zhang,⁵ Qinjun Peng,⁵ Hanqing Mao,¹ Guodong Liu,^{1,2} Jiangping Hu,^{1,2} Youguo Shi,¹ Zuyan Xu,⁵ Kun Jiang,¹ Qingming Zhang,^{1,2} Ziqiang Wang^①,^{6,†} Hongjun Gao,^{1,2,3,4,‡} and X. J. Zhou^①,^{1,2,3,§}

¹Beijing National Laboratory for Condensed Matter Physics, *Institute of Physics, Chinese Academy of Sciences, Beijing 100190, China*

²University of Chinese Academy of Sciences, Beijing 100049, China

³Songshan Lake Materials Laboratory, Dongguan 523808, China

⁴CAS Center for Excellence in Topological Quantum Computation, *University of Chinese Academy of Sciences, Beijing 100190, China*

⁵Technical Institute of Physics and Chemistry, Chinese Academy of Sciences, Beijing 100190, China

⁶Department of Physics, *Boston College, Chestnut Hill, Massachusetts 02467, USA*



(Received 4 August 2024; revised 26 March 2025; accepted 2 April 2025; published 14 April 2025)

The newly discovered kagome superconductors AV_3Sb_5 ($A = K, Rb,$ and Cs) continue to bring surprises in generating unusual phenomena and physical properties, including the anomalous Hall effect, unconventional charge density wave, electronic nematicity, and time-reversal symmetry breaking. Here we report an unexpected emergence of multiple flat band-like nondispersive features in the AV_3Sb_5 superconductors. By performing high-resolution angle-resolved photoemission (ARPES) measurements, we observed four branches of nondispersive features that span over the entire momentum space. The appearance of the nondispersive features is not anticipated from the band structure calculations and cannot be accounted for by the known mechanisms of flat band generation. It is intimately related to the evolution of Van Hove singularities. Here we observe such emergence of multiple nondispersive features in solid materials. Our findings provide insights in revealing the underlying mechanism that governs the unusual behaviors in the kagome superconductors. They also provide a pathway in producing nondispersive features and set a platform to study flat band related physics.

DOI: [10.1103/PhysRevB.111.155123](https://doi.org/10.1103/PhysRevB.111.155123)

I. INTRODUCTION

The kagome lattice, with corner-sharing triangle networks, engenders characteristic electronic structures with Van Hove singularities (VHSs) at the Brillouin zone boundary, a Dirac cone at the zone corner, and a flat band through the entire momentum space [1,2]. Such unique electronic structures facilitate the exploration of a plethora of novel phenomena such as the quantum spin liquid phase, nontrivial topology, superconductivity, and other correlated phenomena [1–12]. The newly discovered kagome superconductors AV_3Sb_5 ($A = K, Rb,$ and Cs) [13,14] have immediately attracted tremendous interest because they generate abundant quantum states and physical properties including the giant anomalous Hall effect without long-range magnetic order [15,16], unconventional charge and pair density waves [17–20], electronic nematicity [21], time-reversal symmetry breaking [22,23], and possible unconventional superconductivity [19,22,24–27]. Understanding these novel quantum phenomena requires thorough investigations on the electronic structures of AV_3Sb_5 systems.

On the other hand, the flat band systems have emerged as a fertile playground in condensed matter physics exemplified by twisted bilayer graphene [28–30]. The flat bands are characterized by quenched kinetic energy, singular density of states, electron correlation, and localization. Plenty of Coulomb interaction-driven many-body states are expected in flat band systems, such as ferromagnetism [31,32], superconductivity [33,34], Wigner crystals [35], and quantum Hall states [36–39]. Theoretically, the flat bands are predicted mainly based on two origins: the localized atomic orbitals and some peculiar lattice geometries [31,32,34,40–43]. However, the experimental observation of flat bands has become possible only recently and its realization is limited to a few systems such as heavy-fermion materials [44], kagome compounds [45,46], and twisted bilayer graphene [28,47,48].

We carried out angle-resolved photoemission (ARPES) measurements by using our laboratory-based laser ARPES system (see Methods section below). We systematically measured AV_3Sb_5 ($A = K, Rb,$ and Cs) (abbreviated as KVS, RVS, and CVS, respectively) and Ti-substituted $CsV_{3-x}Ti_xSb_5$ ($x = 0.04, 0.15,$ and 0.27) [abbreviated as CVS(0.04), CVS(0.15), and CVS(0.27), respectively] samples (see Methods). AV_3Sb_5 exhibit charge density wave (CDW) transitions at ~ 80 K in KV_3Sb_5 , ~ 102 K in RbV_3Sb_5 , and ~ 93 K in CsV_3Sb_5 [13,14,49,50,51]. The Ti substitution in $CsV_{3-x}Ti_xSb_5$ introduces holes and suppresses the CDW transition [51].

*These authors contributed equally to this work.

†Contact author: ziqiang.wang@bc.edu

‡Contact author: hjgao@iphy.ac.cn

§Contact author: xjzhou@iphy.ac.cn

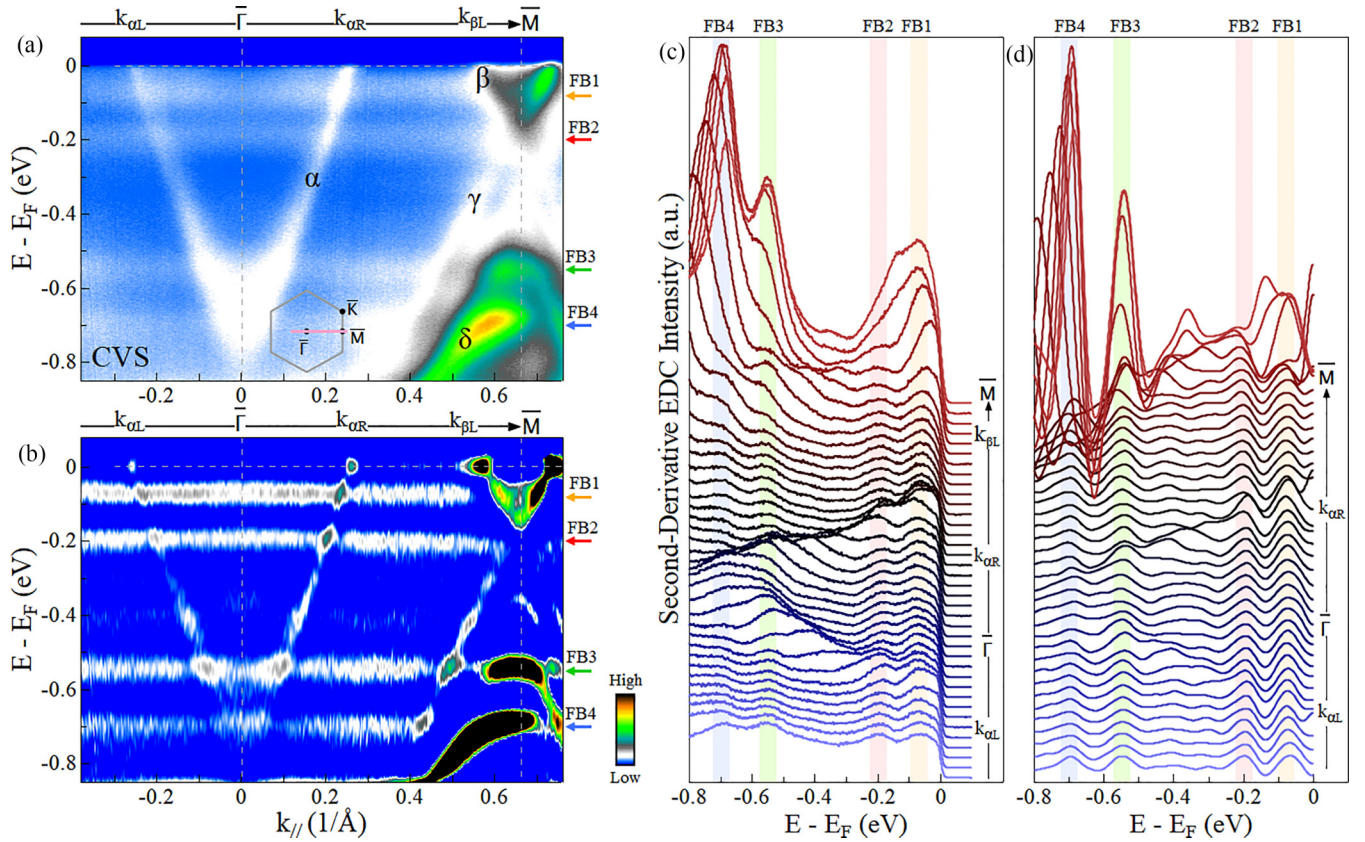


FIG. 1. Observation of multiple flat bands over the entire momentum space in CsV_3Sb_5 . (a) Band structure measured at 20 K along the $\bar{\Gamma} - \bar{M}$ direction. The location of the momentum cut is marked as a solid pink line in the inset. (b) The corresponding second-derivative image with respect to energy obtained from (a). The four arrows on the right side of (a) and (b) are guides to the eye for the observed flat bands. (c) The corresponding photoemission spectra (energy distribution curves, EDCs) from the band structure in (a). The momentum range where the EDCs are extracted is marked as a black arrow on the top of (a). The EDCs extracted at the Fermi momenta ($k_{\alpha L}$, $k_{\alpha R}$, and $k_{\beta L}$) and high-symmetry points ($\bar{\Gamma}$ and \bar{M}) are marked. Four vertical shaded regions at the binding energies of 70 meV (FB1), 200 meV (FB2), 550 meV (FB3), and 700 meV (FB4) are guides to the eye for the flat bands. (d) The corresponding second-derivative EDCs from the second-derivative image in (b). The momentum range where the second-derivative EDCs are extracted is marked as a black arrow on the top of (b).

The $\text{CsV}_{3-x}\text{Ti}_x\text{Sb}_5$ ($x = 0.04$) exhibits a CDW transition at ~ 63 K, while the CDW transition is undetectable in the $\text{CsV}_{3-x}\text{Ti}_x\text{Sb}_5$ ($x = 0.15$ and $x = 0.27$) samples [51].

II. RESULTS

Figure 1 shows the band structure of CsV_3Sb_5 measured along the $\bar{\Gamma} - \bar{M}$ high-symmetry direction at 20 K. In addition to the original α band around $\bar{\Gamma}$ and β , γ , and δ bands around \bar{M} [14,50], four dispersionless features are clearly observed that span the entire measured momentum space, as marked by arrows and labeled as FB1–FB4 in Fig. 1(a). These features show up more clearly in the second-derivative images in Fig. 1(b). Their energy positions are at the binding energies of ~ 70 meV (FB1), ~ 200 meV (FB2), ~ 550 meV (FB3), and ~ 700 meV (FB4). The presence of these nondispersive features can also be observed in the photoemission spectra (energy distribution curves, EDCs) [Fig. 1(c)] and becomes more evident in the corresponding second-derivative EDCs [Fig. 1(d)].

The observation of these multiple nondispersive features is unexpected because no such bands are present in the calculated band structures [13,50]. In our ARPES measure-

ments with ~ 15 μm spot size, we observed various regions with different intensities of the folded bands (Fig. S1 in the Supplemental Material [52]) related to the CDW order and surface reconstructions of different cleaved surfaces [19,50,53]. However, the nondispersive features can be observed both in regions with strong band foldings and in regions with little band foldings (Fig. S1 in the Supplemental Material [52]), indicating that they are not induced by the bulk CDW or surface reconstructions. These nondispersive features are robust and can be observed in measurements under different polarization geometries (Fig. S2 in the Supplemental Material [52]). Furthermore, they are observed not only along the $\bar{\Gamma} - \bar{M}$ direction, but also along the $\bar{\Gamma} - \bar{K}$ and non-high-symmetry directions (Figs. S3–S5 in the Supplemental Material [52]), thus covering the entire two-dimensional Brillouin zone.

Here we observe multiple nondispersive features in AV_3Sb_5 ; they were not observed in the previous ARPES measurements [54–57]. This is mainly because we used UV laser to carry out the ARPES measurements. By using UV laser, the relative intensity of the nondispersive features appears to be enhanced compared with using other photon energies. This is due to photoemission matrix element effects [58]. It

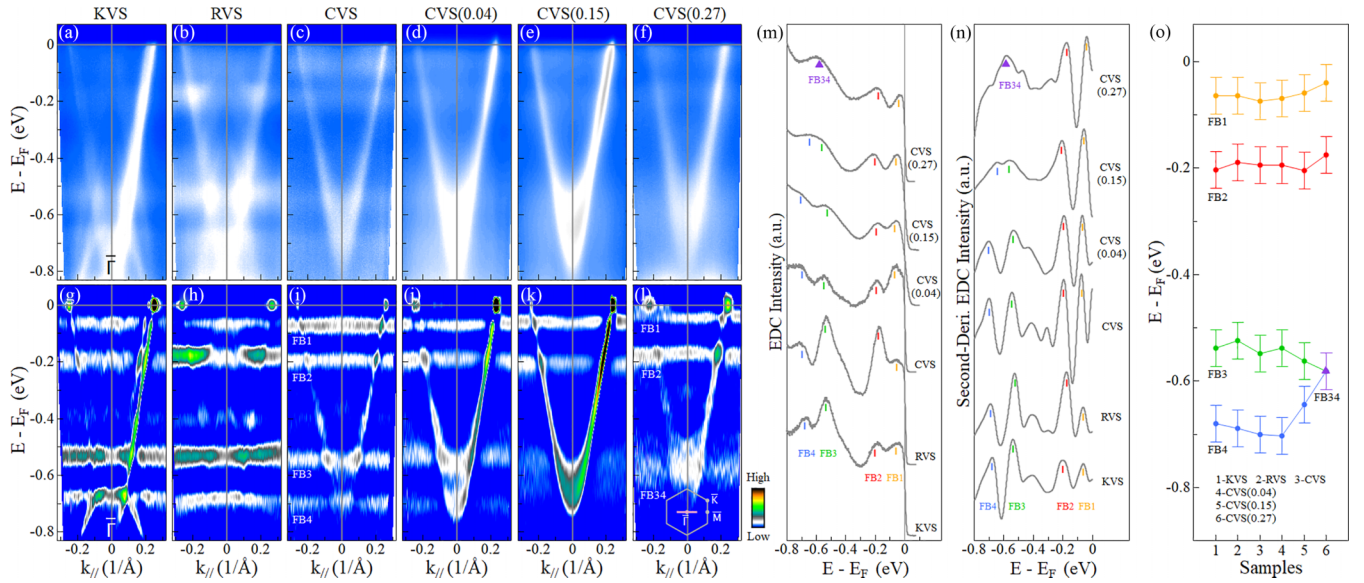


FIG. 2. Multiple flat bands in AV_3Sb_5 ($A = K, Rb,$ and Cs) and their doping dependence. (a)–(f) Band structures measured at 20 K along the $\bar{M} - \bar{\Gamma} - \bar{M}$ direction in KV_3Sb_5 (KVS) (a), RbV_3Sb_5 (RVS) (b), CsV_3Sb_5 (CVS) (c), $CsV_{3-x}Ti_xSb_5$ ($x = 0.04$) [CVS(0.04)] (d), $CsV_{3-x}Ti_xSb_5$ ($x = 0.15$) [CVS(0.15)] (e), and $CsV_{3-x}Ti_xSb_5$ ($x = 0.27$) [CVS(0.27)] (f). The location of the momentum cuts for (a)–(f) is marked as a solid pink line in the inset of (l). (g)–(l) The corresponding second-derivative images with respect to energy obtained from (a)–(f). (m) EDCs extracted at $k_{||} = -0.27$ $1/\text{\AA}$ from (a)–(f). This momentum point is chosen to highlight the contribution from the flat bands because it is away from the original and folded bands. FB1–FB4 and FB34 mark the position of the flat bands. In each EDC, the position of the flat bands is marked by bars or triangles. (n) Second-derivative EDCs extracted at $k_{||} = -0.27$ $1/\text{\AA}$ from (g)–(l). (o) Sample-dependent and doping-dependent energy positions of the observed flat bands. Samples 1–6 represent KVS, RVS, CVS, CVS(0.04), CVS(0.15), and CVS(0.27), respectively, as marked on the bottom. The error bars reflect the uncertainty in determining the energy positions of the flat bands.

is common that for different materials some particular photon energies are preferred to enhance photoemission signals, like ~ 55 eV used for $(La, Sr)_2CuO_4$ [59], 40.8 eV used for 4f bands in Ce films [60], 16.5 eV used for $(Nd_{2-x}Ce_x)CuO_4$ [61], and 19.4 eV for $HgBa_2CuO_{4+\delta}$ [62]. Since our laser ARPES can see these four flat bands clearly, it provides sufficient evidence on their existence in AV_3Sb_5 .

The nondispersive features are observed in the AV_3Sb_5 ($A = K, Rb,$ and Cs) compounds and show a peculiar doping dependence in $CsV_{3-x}Ti_xSb_5$ ($x = 0 \sim 0.27$). Figure 2 shows the band structures measured at 20 K along the $\bar{M} - \bar{\Gamma} - \bar{M}$ direction in KV_3Sb_5 [Fig. 2(a)], RbV_3Sb_5 [Fig. 2(b)], CsV_3Sb_5 [Fig. 2(c)], $CsV_{3-x}Ti_xSb_5$ ($x = 0.04$) [Fig. 2(d)], $CsV_{3-x}Ti_xSb_5$ ($x = 0.15$) [Fig. 2(e)], and $CsV_{3-x}Ti_xSb_5$ ($x = 0.27$) [Fig. 2(f)] samples. The corresponding second-derivative images are shown in Figs. 2(g)–2(l). The EDCs for different samples at a particular momentum away from the main bands are presented in Fig. 2(m), with contributions mainly from the nondispersive features. The corresponding second-derivative EDCs are presented in Fig. 2(n). The multiple nondispersive features are clearly observed in all the parent AV_3Sb_5 ($A = K, Rb,$ and Cs) compounds with similar energy scales. Upon hole doping through Ti substitution in $CsV_{3-x}Ti_xSb_5$, the FB1 and FB2 bands remain pronounced with only a slight energy position variation due to hole-doping-induced chemical potential shift. In contrast, the FB3 and FB4 bands exhibit a dramatic change with the hole doping. With increased hole doping, the FB3 and FB4 bands become weaker in the spectral intensity, shrink in their energy separation, and eventually merge into a single nondispersive

feature FB34 at the high doping in the CVS(0.27) sample. The quantitative energy position variation of the nondispersive features in these samples is summarized in Fig. 2(o). It has been found that the hole doping in $CsV_{3-x}Ti_xSb_5$ suppresses the CDW transition which is completely undetectable in the high-doping CVS(0.27) sample [51]. The observed doping evolution of the FB3 and FB4 nondispersive features is closely related to the doping evolution of the CDW transition in $CsV_{3-x}Ti_xSb_5$.

In order to further check on the relation between the nondispersive features and the CDW transition, we carried out temperature-dependent measurements on RbV_3Sb_5 across the CDW transition temperature of ~ 102 K. Figure 3 shows the band structures of RbV_3Sb_5 measured along the $\bar{M} - \bar{\Gamma} - \bar{M}$ direction at different temperatures. The corresponding EDCs and the second-derivative EDCs at a particular momentum are presented in Figs. 3(b) and 3(c), respectively. As seen in Fig. 3, the FB1 and FB2 nondispersive features are observed in the entire temperature range of $20 \sim 170$ K. Their energy positions show little temperature dependence when crossing the CDW transition. On the other hand, the FB3 and FB4 nondispersive features exhibit a dramatic evolution with temperature. With the increasing temperature, the spectral intensity of these two nondispersive features gets weaker, the energy separation between them gets smaller, and eventually these two nondispersive features FB3 and FB4 merge into one nondispersive feature FB34 at temperatures above the CDW transition temperature of ~ 102 K. We checked the reversibility of the nondispersive features after heating and cooling processes. The nondispersive features FB3 and FB4 reappear

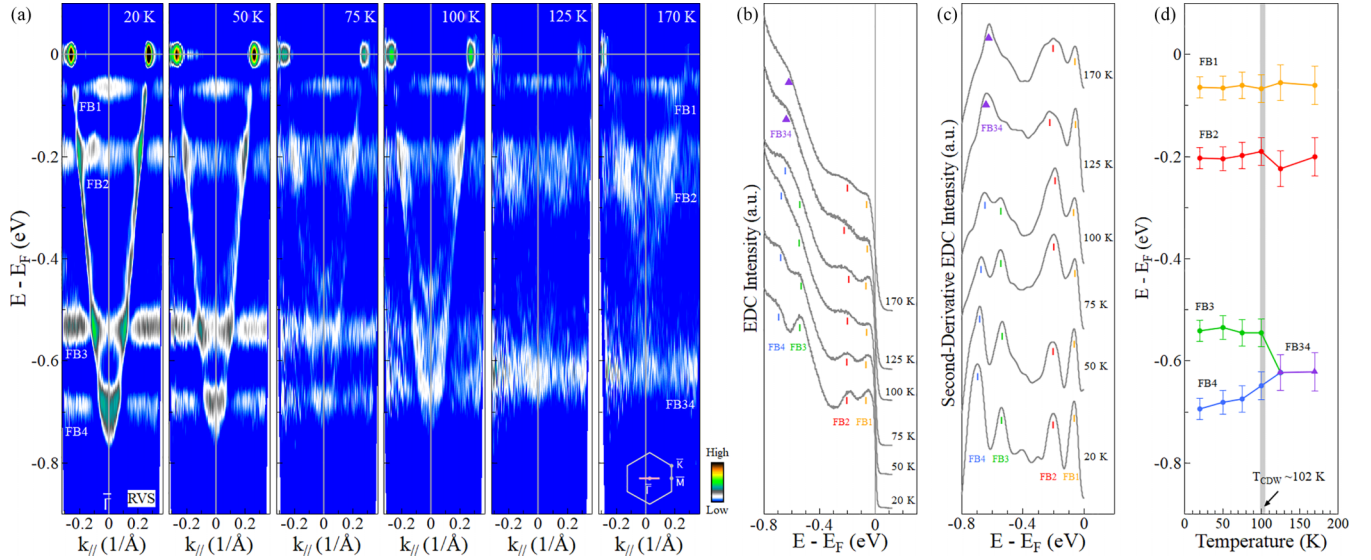


FIG. 3. Evolution of the flat bands with temperature in RbV_3Sb_5 . (a) Band structures measured at different temperatures from 20 K to 170 K along the $\bar{M} - \bar{\Gamma} - \bar{M}$ direction. The location of the momentum cut is marked as a solid pink line in the inset of the rightmost panel. These are second-derivative images with respect to energy obtained from the original data. (b) The EDCs at $k_{||} = +0.30$ 1/Å measured at different temperatures extracted from the original data. (c) The corresponding second-derivative EDCs at $k_{||} = +0.30$ 1/Å measured at different temperatures extracted from (a). FB1–FB4 and FB34 indicate the energy positions of the flat bands. In each EDC, the positions of the flat bands are marked by bars or triangles in different colors. (d) Temperature-dependent energy positions of the flat bands. The error bars reflect the uncertainty in determining the energy positions of the flat bands.

when the temperature goes back below the CDW transition temperature. The energy position evolution with temperature for the nondispersive features is summarized in Fig. 3(d). The temperature dependence of the nondispersive features shows a strong resemblance to the doping dependence shown in Fig. 2. These strongly indicate that the origin of the FB3 and FB4 nondispersive features is closely related to the CDW transition.

In order to understand the origin of the nondispersive features, we compared their energy positions with those original bands and found that the emergence of the nondispersive features is closely related to the Van Hove singularities at the \bar{M} point. Figure 4(a) shows the band structure of CsV_3Sb_5 measured along the $\bar{\Gamma} - \bar{M}$ direction at 20 K in the CDW state. This measurement covers both the nondispersive features and the original bands at the \bar{M} point, making their direct comparison possible. As seen from the band structure calculations in Fig. 4(b), in the CDW state, three Van Hove singularities (vHs1, vHs2, and vHs3) are present at \bar{M} . Each Van Hove singularity splits in energy and forms an upper branch (vHs1u, vHs2u, and vHs3u) and a lower branch (vHs1l, vHs2l, and vHs3l). The observed bands at \bar{M} in Fig. 4(a) show a good correspondence to those in Fig. 4(b), as labeled on the right of Fig. 4(a). These results are consistent with the previous band structure calculations and ARPES measurements of VHSs in CsV_3Sb_5 [54]. Figure 4(c) shows the second-derivative EDCs measured at $k_{||} = -0.27$ 1/Å in Fig. 4(a) highlighting the contribution of the nondispersive features and at $k_{||} = +0.66$ 1/Å in Fig. 4(a) emphasizing the contribution of the original bands at \bar{M} . The energy positions of the flat bands exhibit a good correspondence to those of the Van Hove singularity bands. When it comes to the $\text{CsV}_{3-x}\text{Ti}_x\text{Sb}_5$ ($x = 0.27$) sample with high hole

doping without CDW transition, there remain three Van Hove singularities expected at \bar{M} [Fig. 4(e)]. However, the vHs3 does not split although vHs1 and vHs2 keep splitting at \bar{M} . The expected three bands can be clearly observed in Fig. 4(d) at \bar{M} as marked on its right side. Figure 4(f) shows the second-derivative EDCs measured at $k_{||} = -0.27$ 1/Å and at \bar{M} from Fig. 4(d). Again, the energy positions of the nondispersive features shows an excellent agreement with those of the Van Hove singularity bands. These results strongly indicate that the emergence of the nondispersive features is intimately linked to the band structures at \bar{M} , particularly the Van Hove singularities.

III. DISCUSSION

Flat band systems, constituted by localized or dressed heavy electrons with large effective masses, are an ideal platform to explore correlated electronic phenomena, such as magnetism and unconventional superconductivity [28,29,63]. There are several mechanisms that can produce the dispersionless extension of spectral intensity in the momentum space. When electrons are localized within atoms and the electron hopping is limited, a flat band can be formed, such as the 4f electrons in heavy-fermion materials [Fig. 4(g)] [63]. In some special lattice geometries, like in the kagome lattice [Fig. 4(h)], the flat band can be formed due to destructive interference [29]. In addition, we note that there are two other ways to produce flat band-like features. In the case of electron coupling with a bosonic mode, a flat band-like feature may appear at the mode energy Ω_0 [Fig. 4(i); see Fig. S6 in the Supplemental Material [52]] [64]. In the case of electron-mode coupling with the presence of a VHS, a flat band-like feature may emerge at $\Omega_0 + E$ with E being

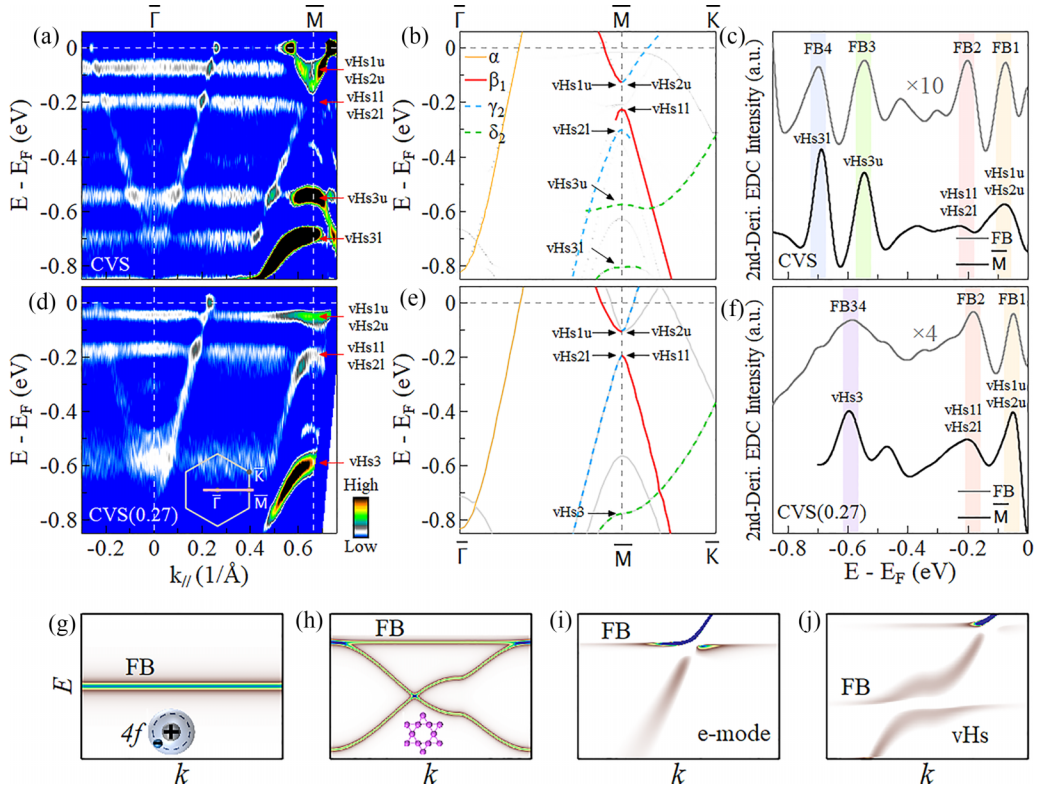


FIG. 4. The relation between the flat bands and the Van Hove singularities and the origins of flat bands. (a) and (d): Band structures measured at 20 K along the $\bar{\Gamma} - \bar{M}$ direction in CsV_3Sb_5 (a) and $\text{CsV}_{3-x}\text{Ti}_x\text{Sb}_5$ ($x = 0.27$) (d). The location of the momentum cuts is marked as a solid pink line in the inset of (d). These are second-derivative images with respect to energy obtained from original data. (b) and (e): Calculated band structures along the $\bar{\Gamma} - \bar{M} - \bar{K}$ direction in CsV_3Sb_5 with the reconstructed TrH crystal structure [83] (b) and with pristine crystal structure (e) at $k_z = \pi/c$ without spin-orbit coupling. The Van Hove singularities (vHs1, vHs2, and vHs3) are marked by arrows which are associated with the β_1 , γ_2 , and δ_2 bands, respectively, that are highlighted by colored lines. When a Van Hove singularity splits at \bar{M} , the two branches are labeled with suffixes u (upper) and l (lower) such as vHs3u and vHs3l. (c) Second-derivative EDCs at $k_{\parallel} = +0.30 \text{ 1/\AA}$ (gray line) contributed mainly from the flat bands and at \bar{M} (black line) contributed mainly from the Van Hove singularities, extracted from (a). For comparison, the second-derivative EDC at $k_{\parallel} = +0.30 \text{ 1/\AA}$ is multiplied by 10 in intensity. (f) Same as (c) but extracted from (d). (g) Flat bands in heavy-fermion materials. (h) The flat band in the kagome lattice. (i) The flat band-like feature in electron-mode coupling [64]. This is the EDC second-derivative image; the original image is shown in Fig. S6 in the Supplemental Material [52]. (j) The flat band-like feature coming from Van Hove singularity in an electron-mode coupling system. This is the EDC second-derivative image; the original image is shown in Fig. S7 in the Supplemental Material [52].

the binding energy of the VHS [Fig. 4(j); see Fig. S7 in the Supplemental Material [52]] [65].

Our measured results provide important information on understanding the origin of these nondispersive features. Since multiple nondispersive features are observed in AV_3Sb_5 and their energies coincide with those of VHSs, this rules out the possibility that these nondispersive features come from impurity bands [66–68]. This can also exclude the possibility of localized atomic orbital bands [Fig. 4(g)]. One possibility is whether these nondispersive features may come from the scattering of electrons at the VHSs by impurities or disorders. To the best of our knowledge, such phenomena have not been observed in the previous ARPES measurements of materials with VHSs [45,69]. There are several results that are not consistent with this scenario. First, the intensity of the nondispersive features is not proportional to the intensity of the Van Hove singularities. As seen in Fig. S2c, although the intensity of vHs11/vHs2l is much weaker than that of vHs3u and vHs3l, the intensity of the nondispersive feature FB2 is comparable to that of the nondispersive features FB3 and FB4. Second, as

seen in Fig. S2d, when the polarization changes from LV to LH, although the intensity of vHs3u dramatically decreases, the intensity of the nondispersive feature FB3 is nearly the same. Third, although the cleaved sample surface consists of different regions, like Cs-terminated, half Cs-terminated, and Sb-terminated in CsV_3Sb_5 [19], we always observe similar nondispersive features, even in regions with strong band foldings and in regions with little band foldings (Fig. S1 in the Supplemental Material [52]). These results indicate that the electron scattering by surface alkali metal adatoms or vacancies generated upon cleaving cannot provide a consistent explanation of the nondispersive features we observed.

In addition, our observed nondispersive features are not induced by the destructive interference of wave functions in the kagome lattice [Fig. 4(h)] because they are expected to be $\sim 1 \text{ eV}$ away from the Fermi level from the band structure calculations in AV_3Sb_5 [54,55], which is apparently different from our observations. Electron-mode coupling can produce flat band-like feature [Fig. 4(i)]. However, our observation of four nondispersive features is unlikely due to such electron-

mode coupling because no collective excitations with similar energy scales have been observed in AV_3Sb_5 . Furthermore, in the electron-mode coupling picture [Fig. 4(i)], the spectral weight of the flat band-like feature decays rapidly with the momentum moving away from the main band. This is inconsistent with our observation that the spectral weight of the flat bands changes little in the wide momentum space. It is also highly unlikely to have four bosonic modes which have similar energies to the VHS and particularly strong electron-mode coupling which will make the Migdal theory break down. In the case of electron-mode coupling with a coexisting VHS, the flat band-like feature can also occur near the energy position of the VHS [Fig. 4(j)]. This scenario closely connects the flat band-like feature with the VHS which is consistent with our observations. But similarly to the electron-mode coupling case, the flat band-like feature loses its spectral weight rapidly with the momentum moving away from the VHS. This is not consistent with the nearly uniform momentum distribution of the flat bands we observed. We have discussed all possible origins of the flat bands that have been known so far and compared with our observations. We found that none of these known scenarios can satisfactorily explain the appearance of multiple nondispersive features in AV_3Sb_5 . We note that a near-Fermi-level nondispersive feature, which is similar to FB1, was observed in synchrotron-ARPES data, but the underlying mechanism is still elusive. A similar origin may be found upon further exploration [70]. Based on all the above considerations, a possible interpretation is that a coherent spectral weight originates from the Van Hove singularities, which is a driving force for many surprising properties. The presence of the flat band-like nondispersive features suggests a potential role of many-body interactions in modifying the band dispersion, which merits further exploration.

IV. CONCLUSION

In summary, we have discovered the emergence of multiple nondispersive features in AV_3Sb_5 . These observations are unexpected and the origin of these nondispersive features cannot be understood by the known mechanisms of flat band generation. The occurrence of these nondispersive features is clearly associated with the Van Hove singularities, which may be further related to their singular density of states. The Van Hove singularities have been reported in a number of systems, but the VHS-driven generation of the nondispersive features has now been observed in AV_3Sb_5 . These indicate that some unusual mechanisms are at play in AV_3Sb_5 , like the discovery of the unexpected anomalous Hall effect in this system. Our work provides a paradigm to generate nondispersive features and will stimulate further efforts to understand the origin of flat bands and other unusual phenomena in kagome superconductors.

Methods

Growth and characterization of single crystals. High-quality single crystals of AV_3Sb_5 ($A = K, Rb, \text{ and } Cs$) and $CsV_{3-x}Ti_xSb_5$ ($x = 0.04, 0.15, \text{ and } 0.27$) were grown from modified self-flux methods [13,51]. The crystals were characterized by x-ray diffraction, STM, and EELS, as well

as measurements of the magnetic susceptibility and electrical resistance [50,51]. AV_3Sb_5 exhibit CDW transitions at ~ 80 K (KV_3Sb_5), ~ 102 K (RbV_3Sb_5), and ~ 93 K (CsV_3Sb_5) [13,14,49,50,51], respectively. The Ti substitution for V in $CsV_{3-x}Ti_xSb_5$ crystals has been confirmed by scanning transmission electron microscopy, electron energy-loss spectroscopy, and scanning tunneling microscopy [51]. $CsV_{3-x}Ti_xSb_5$ ($x = 0.04$) exhibits a CDW transition at ~ 63 K while no CDW transition is observed in the $CsV_{3-x}Ti_xSb_5$ ($x = 0.15$ and $x = 0.27$) samples [51].

High-resolution ARPES measurements. High-resolution angle-resolved photoemission measurements were carried out on our laboratory system equipped with a Scienta DA30L electron energy analyzer [71,72]. We use ultraviolet laser as the light source that can provide a photon energy of $h\nu = 6.994$ eV with a bandwidth of 0.26 meV. The energy resolution was set at ~ 2.5 meV. The angular resolution is $\sim 0.3^\circ$, corresponding to a momentum resolution of ~ 0.004 1/Å for the photon energy of 6.994 eV. The laser spot size is set at ~ 15 μm. The Fermi level is referenced by measuring on a clean polycrystalline gold that is electrically connected to the sample. The sample was cleaved *in situ* and measured in vacuum with a base pressure better than 5×10^{-11} Torr.

Band structure calculations. First-principles calculations are performed by using the projected augmented wave method (PAW) density functional theory (DFT), as implemented in the Vienna *Ab initio* Simulation Package (VASP) [73–75]. A $2 \times 2 \times 1$ supercell is constructed to describe the trihexagonal (TrH) CDW phase of AV_3Sb_5 . The crystal structures are relaxed by using the Perdew-Burke-Ernzerhof (PBE) functional [76] and zero-damping DFT-D3 van der Waals correction [77] until the forces are less than 0.001 eV/Å. The cutoff energy of the plane wave basis is set at 600 eV and the energy convergence criterion is set at 10^{-7} eV. The corresponding Brillouin zones are sampled by using a $16 \times 16 \times 10$ (for the primitive cell) and a $8 \times 8 \times 10$ (for the supercell) Γ -centered \mathbf{k} grid. The effective band structure is calculated by the band-unfolding method [78,79] proposed by Zunger *et al.* with the BandUP code [80,81]. The $2 \times 2 \times 1$ TrH CDW order reconstruction is an input in our band-unfolding calculation. All the DFT calculations are *ab initio* without any adjustable parameters except for the standard exchange-correlation functional and pseudopotentials.

Spectral function simulation of the electron-mode coupling. We performed a simulation of the single-particle spectral function considering the electron coupling with a bosonic mode. The purpose here is to illustrate the emergence of the flat band-like feature in the case of electron-mode coupling with a coexisting VHS. We follow the fashion of the Migdal theory [82] and calculate the Migdal electron-mode self-energy Σ_{ep} :

$$\Sigma_{ep}(\mathbf{k}, i\omega_n) = \frac{1}{N} \sum_{\mathbf{q}} |g_{\mathbf{k},\mathbf{q}}|^2 \left(\frac{b(\Omega_{\mathbf{q}}) + f(\epsilon_{\mathbf{k}+\mathbf{q}})}{i\omega_n + \Omega_{\mathbf{q}} - \epsilon_{\mathbf{k}+\mathbf{q}}} + \frac{1 + b(\Omega_{\mathbf{q}}) - f(\epsilon_{\mathbf{k}+\mathbf{q}})}{i\omega_n - \Omega_{\mathbf{q}} - \epsilon_{\mathbf{k}+\mathbf{q}}} \right). \quad (1)$$

For simplicity, we consider a case of Einstein mode with constant frequency $\Omega_{\mathbf{q}} \equiv \Omega_0$ and homogeneous electron-

mode coupling constant $g_{\mathbf{k},\mathbf{q}} \equiv g$. Here, $b(\Omega)$ is the Bose-Einstein distribution function, and $f(\epsilon_{\mathbf{k}})$ is the Fermi-Dirac distribution. The spectral function is given by $A(\mathbf{k}, \omega) = -\frac{1}{\pi} \text{Im} G(\mathbf{k}, i\omega_n \rightarrow \omega + i\delta)$, where the Green function $G(\mathbf{k}, i\omega_n) = (i\omega_n - \epsilon_{\mathbf{k}} - \Sigma_{\text{ep}})^{-1}$. In the simulation, we take the case of a square lattice, and the dispersion $\epsilon_{\mathbf{k}} = 2t(\cos k_x + \cos k_y)$. The cut is along the high-symmetry line Γ -X-M. The VHS at X = $(\pi, 0)$ is placed at the energy of -0.4 eV. The mode frequency Ω_0 is set to be 30 meV and the coupling constant is $g = 0.2$. The simulated results are shown in Fig. S7 in the Supplemental Material [52] and in Fig. 4(j).

ACKNOWLEDGMENTS

This work is supported by the National Natural Science Foundation of China (Grants No. 12488201, No. 61888102, No. 11974404, No. 12074411, and No. U2032204), the National Key Research and Development Program of China (Grants No. 2021YFA1401800, No. 2022YFA1403900, and No. 2018YFA0704200), the Strategic Priority Research Program (B) of the Chinese Academy of Sciences (Grants No. XDB25000000, No. XDB28000000, and No.

XDB33000000), the Innovation Program for Quantum Science and Technology (Grant No. 2021ZD0301800), the Youth Innovation Promotion Association of CAS (Grant No. Y2021006), the U.S. Department of Energy, Basic Energy Sciences (Grant No. DE-FG02-99ER45747), the K. C. Wong Education Foundation (Grant No. GJTD-2018-01), and the Synergetic Extreme Condition User Facility (SECUF).

X.J.Z., H.J.G., L.Z., and H.L.L. conceived this project. H.L.L. performed ARPES experiments and analyzed the ARPES data. Z.Z., H.T.Y., C.M.S., and H.J.G. contributed to crystal growth of pure CsV_3Sb_5 and Ti-doped CsV_3Sb_5 . H.X.L. and Y.G.S. contributed to crystal growth of KV_3Sb_5 , RbV_3Sb_5 , and pure CsV_3Sb_5 . Y.P.H., Y.H.G., J.P.H., K.J., and Z.Q.W. contributed to DFT calculations and theoretical analysis. F.J. and Q.M.Z. contributed to Raman measurements and analysis. L.Z., H.C., C.H.Y., T.M.M., X.L.R., B.L., Y.J.S., Y.W.C., H.Q.M., G.D.L., and X.J.Z. contributed to the development and maintenance of the ARPES systems and related software development. H.L.L., F.F.Z., F.Y., S.J.Z., Q.J.P., and Z.Y.X. contributed to the maintenance of the 7 eV laser system. H.L.L., L.Z., and X.J.Z. wrote this paper with information from all co-authors. All authors participated in discussion and comment on the paper.

-
- [1] H. M. Guo and M. Franz, Topological insulator on the kagome lattice, *Phys. Rev. B* **80**, 113102 (2009).
- [2] A. O'Brien, F. Pollmann, and P. Fulde, Strongly correlated fermions on a kagome lattice, *Phys. Rev. B* **81**, 235115 (2010).
- [3] W. H. Ko, P. A. Lee, and X. G. Wen, Doped kagome system as exotic superconductor, *Phys. Rev. B* **79**, 214502 (2009).
- [4] W.-S. Wang, Z.-Z. Li, Y.-Y. Xiang, and Q.-H. Wang, Competing electronic orders on kagome lattices at van Hove filling, *Phys. Rev. B* **87**, 115135 (2013).
- [5] S. Yan, D. A. Huse, and S. R. White, Spin-liquid ground state of the $S = 1/2$ kagome Heisenberg antiferromagnet, *Science* **332**, 1173 (2011).
- [6] M. R. Norman, *Colloquium: Herbertsmithite and the search for the quantum spin liquid*, *Rev. Mod. Phys.* **88**, 041002 (2016).
- [7] Y. Zhou, K. Kanoda, and T. K. Ng, Quantum spin liquid states, *Rev. Mod. Phys.* **89**, 025003 (2017).
- [8] H. Yang, Y. Sun, Y. Zhang, W. J. Shi, S. S. P. Parkin, and B. Yan, Topological Weyl semimetals in the chiral antiferromagnetic materials Mn_3Ge and Mn_3Sn , *New J. Phys.* **19**, 015008 (2017).
- [9] A. Rüegg and G. A. Fiete, Fractionally charged topological point defects on the kagome lattice, *Phys. Rev. B* **83**, 165118 (2011).
- [10] S. V. Isakov, S. Wessel, R. G. Melko, K. Sengupta, and Y. B. Kim, Hard-core bosons on the kagome lattice: Valence-bond solids and their quantum melting, *Phys. Rev. Lett.* **97**, 147202 (2006).
- [11] M. L. Kiesel and R. Thomale, Sublattice interference in the kagome Hubbard model, *Phys. Rev. B* **86**, 121105 (2012).
- [12] M. L. Kiesel, C. Platt, and R. Thomale, Unconventional Fermi surface instabilities in the kagome Hubbard model, *Phys. Rev. Lett.* **110**, 126405 (2013).
- [13] B. R. Ortiz, L. C. Gomes, J. R. Morey, M. Winiarski, M. Bordelon, J. S. Mangum, I. W. H. Oswald, J. A. Rodriguez-Rivera, J. R. Neilson, S. D. Wilson, E. Ertekin, T. M. McQueen, and E. S. Toberer, New kagome prototype materials: Discovery of KV_3Sb_5 , RbV_3Sb_5 , and CsV_3Sb_5 , *Phys. Rev. Mater.* **3**, 094407 (2019).
- [14] B. R. Ortiz, S. M. L. Teicher, Y. Hu, J. L. Zuo, P. M. Sarte, E. C. Schueller, A. M. M. Abeykoon, M. J. Krogstad, S. Rosenkranz, R. Osborn, R. Seshadri, L. Balents, J. He, and S. D. Wilson, CsV_3Sb_5 : A \mathbb{Z}_2 topological kagome metal with a superconducting ground state, *Phys. Rev. Lett.* **125**, 247002 (2020).
- [15] S. Yang, Y. Wang, B. R. Ortiz, D. Liu, J. Gayles, E. Derunova, R. Gonzalez-Hernandez, L. Šmejkal, Y. Chen, S. S. P. Parkin, S. D. Wilson, E. S. Toberer, T. McQueen, and M. N. Ali, Giant, unconventional anomalous Hall effect in the metallic frustrated magnet candidate, KV_3Sb_5 , *Sci. Adv.* **6**, eabb6003 (2020).
- [16] F. H. Yu, T. Wu, Z. Y. Wang, B. Lei, W. Z. Zhuo, J. J. Ying, and X. H. Chen, Concurrence of anomalous Hall effect and charge density wave in a superconducting topological kagome metal, *Phys. Rev. B* **104**, L041103 (2021).
- [17] Y.-X. Jiang, J.-X. Yin, M. M. Denner, N. Shumiya, B. R. Ortiz, G. Xu, Z. Guguchia, J. He, M. S. Hossain, X. Liu *et al.*, Unconventional chiral charge order in kagome superconductor KV_3Sb_5 , *Nat. Mater.* **20**, 1353 (2021).
- [18] H. Li, T. T. Zhang, T. Yilmaz, Y. Y. Pai, C. E. Marvinney, A. Said, Q. W. Yin, C. S. Gong, Z. J. Tu, E. Vescovo, C. S. Nelson, R. G. Moore, S. Murakami, H. C. Lei, H. N. Lee, B. J. Lawrie, and H. Miao, Observation of unconventional charge density wave without acoustic phonon anomaly in kagome superconductors AV_3Sb_5 ($A = \text{Rb}, \text{Cs}$), *Phys. Rev. X* **11**, 031050 (2021).
- [19] Z. Liang, X. Hou, F. Zhang, W. Ma, P. Wu, Z. Zhang, F. Yu, J. J. Ying, K. Jiang, L. Shan, Z. Wang, and X. H. Chen, Three-dimensional charge density wave and surface-dependent

- vortex-core states in a kagome superconductor CsV₃Sb₅, *Phys. Rev. X* **11**, 031026 (2021).
- [20] H. Chen, H. Yang, B. Hu, Z. Zhao, J. Yuan, Y. Xing, G. Qian, Z. Huang, G. Li, Y. Ye *et al.*, Roton pair density wave in a strong-coupling kagome superconductor, *Nature (London)* **599**, 222 (2021).
- [21] L. Nie, K. Sun, W. Ma, D. Song, L. Zheng, Z. Liang, P. Wu, F. Yu, J. Li, M. Shan *et al.*, Charge-density-wave-driven electronic nematicity in a kagome superconductor, *Nature (London)* **604**, 59 (2022).
- [22] C. Mielke III, D. Das, J.-X. Yin, H. Liu, R. Gupta, Y.-X. Jiang, M. Medarde, X. Wu, H. C. Lei, J. Chang *et al.*, Time-reversal symmetry-breaking charge order in a kagome superconductor, *Nature (London)* **602**, 245 (2022).
- [23] L. Yu, C. Wang, Y. Zhang, M. Sander, S. Ni, Z. Lu, S. Ma, Z. Wang, Z. Zhao, H. Chen *et al.*, Evidence of a hidden flux phase in the topological kagome metal CsV₃Sb₅, [arXiv:2107.10714](https://arxiv.org/abs/2107.10714).
- [24] C. C. Zhao, L. S. Wang, W. Xia, Q. W. Yin, J. M. Ni, Y. Y. Huang, C. P. Tu, Z. C. Tao, Z. J. Tu, C. S. Gong, H. C. Lei, Y. F. Guo, X. F. Yang, and S. Y. Li, Nodal superconductivity and superconducting domes in the topological kagome metal CsV₃Sb₅, [arXiv:2102.08356](https://arxiv.org/abs/2102.08356).
- [25] W. Duan, Z. Nie, S. Luo, F. Yu, B. R. Ortiz, L. Yin, H. Su, F. Du, A. Wang, Y. Chen, X. Lu, J. Ying, S. D. Wilson, X. Chen, Y. Song, and H. Yuan, Nodeless superconductivity in the kagome metal CsV₃Sb₅, *Sci. China Phys. Mech. Astron.* **64**, 107462 (2021).
- [26] C. Mu, Q. Yin, Z. Tu, C. Gong, H. Lei, Z. Li, and J. Luo, S-wave superconductivity in kagome metal CsV₃Sb₅ revealed by ^{121/123}Sb NQR and ⁵¹V NMR measurements, *Chin. Phys. Lett.* **38**, 077402 (2021).
- [27] H. S. Xu, Y. J. Yan, R. Yin, W. Xia, S. Fang, Z. Chen, Y. Li, W. Yang, Y. Guo, and D. L. Feng, Multiband superconductivity with sign-preserving order parameter in kagome superconductor CsV₃Sb₅, *Phys. Rev. Lett.* **127**, 187004 (2021).
- [28] Y. Cao, V. Fatemi, S. Fang, K. Watanabe, T. Taniguchi, E. Kaxiras, and P. Jarillo-Herrero, Unconventional superconductivity in magic-angle graphene superlattices, *Nature (London)* **556**, 43 (2018).
- [29] Z. Liu, F. Liu, and Y. S. Wu, Exotic electronic states in the world of flat bands: From theory to material, *Chin. Phys. B* **23**, 077308 (2014).
- [30] D. Leykam, A. Andreanov, and S. Flach, Artificial flat band systems: From lattice models to experiments, *Adv. Phys.: X* **3**, 1473052 (2018).
- [31] A. Mielke, Ferromagnetic ground states for the Hubbard model on line graphs, *J. Phys. A: Math. Gen.* **24**, L73 (1991).
- [32] H. Tasaki, Ferromagnetism in the Hubbard models with degenerate single-electron ground states, *Phys. Rev. Lett.* **69**, 1608 (1992).
- [33] S. Miyahara, S. Kusuta, and N. Furukawa, BCS theory on a flat band lattice, *Physica C* **460–462**, 1145 (2007).
- [34] E. S. Morell, J. D. Correa, P. Vargas, M. Pacheco, and Z. Barticevic, Flat bands in slightly twisted bilayer graphene: Tight-binding calculations, *Phys. Rev. B* **82**, 121407(R) (2010).
- [35] C. Wu, D. Bergman, L. Balents, and D. D. Sarma, Flat bands and Wigner crystallization in the honeycomb optical lattice, *Phys. Rev. Lett.* **99**, 070401 (2007).
- [36] E. Tang, J.-W. Mei, and X.-G. Wen, High-temperature fractional quantum Hall states, *Phys. Rev. Lett.* **106**, 236802 (2011).
- [37] T. Neupert, L. Santos, C. Chamon, and C. Mudry, Fractional quantum Hall states at zero magnetic field, *Phys. Rev. Lett.* **106**, 236804 (2011).
- [38] K. Sun, Z. Gu, H. Katsura, and D. S. Sarma, Nearly flatbands with nontrivial topology, *Phys. Rev. Lett.* **106**, 236803 (2011).
- [39] G. Xu, B. Lian, and S. C. Zhang, Intrinsic quantum anomalous Hall effect in the kagome lattice Cs₂LiMn₃F₁₂, *Phys. Rev. Lett.* **115**, 186802 (2015).
- [40] H. Tsunetsugu, M. Sigrist, and K. Ueda, The ground-state phase diagram of the one-dimensional Kondo lattice model, *Rev. Mod. Phys.* **69**, 809 (1997).
- [41] B. Sutherland, Localization of electronic wave functions due to local topology, *Phys. Rev. B* **34**, 5208 (1986).
- [42] E. H. Lieb, Two theorems on the Hubbard model, *Phys. Rev. Lett.* **62**, 1201 (1989).
- [43] N. Regnault, Y. Xu, M.-R. Li, D.-S. Ma, M. Jovanovic, A. Yazdani, S. S. Parkin, C. Felser, L. M. Schoop, N. P. Ong, R. J. Cava, L. Elcore, Z.-D. Song, and B. A. Bernevig, Catalogue of flat-band stoichiometric materials, *Nature (London)* **603**, 824 (2022).
- [44] N. Xu, X. Shi, P. K. Biswas, C. E. Matt, R. S. Dhaka, Y. Huang, N. C. Plumb, M. Radović, J. H. Dil, E. Pomjakushina, K. Conder, A. Amato, Z. Salman, D. McK. Paul, J. Mesot, H. Ding, and M. Shi, Surface and bulk electronic structure of the strongly correlated system SmB₆ and implications for a topological Kondo insulator, *Phys. Rev. B* **88**, 121102(R) (2013).
- [45] M. Kang, L. Ye, S. Fang, J. S. You, A. Levitan, M. Han, J. I. Facio, C. Jozwiak, A. Bostwick, E. Rotenberg *et al.*, Dirac fermions and flat bands in the ideal kagome metal FeSn, *Nat. Mater.* **19**, 163 (2020).
- [46] J. Yang, X. Yi, Z. Zhao, Y. Xie, T. Miao, H. Luo, H. Chen, B. Liang, W. Zhu, Y. Ye *et al.*, Observation of flat band, Dirac nodal lines and topological surface states in kagome superconductor CsTi₃Bi₅, *Nat. Commun.* **14**, 4089 (2023).
- [47] M. I. B. Utama, R. J. Koch, K. Lee, N. Leconte, H. Li, S. Zhao, L. Jiang, J. Zhu, K. Watanabe, T. Taniguchi, P. D. Ashby, A. Weber-Bargioni, A. Zettl, C. Jozwiak, J. Jung, E. Rotenberg, A. Bostwick, and F. Wang, Visualization of the flat electronic band in twisted bilayer graphene near the magic angle twist, *Nat. Phys.* **17**, 184 (2021).
- [48] S. Lisi, X. Lu, T. Benschop, T. A. de Jong, P. Stepanov, J. R. Duran, F. Margot, I. Cucchi, E. Cappelli, A. Hunter *et al.*, Observation of flat bands in twisted bilayer graphene, *Nat. Phys.* **17**, 189 (2021).
- [49] Q. Yin, Z. Tu, C. Gong, Y. Fu, S. Yan, and H. Lei, Superconductivity and normal-state properties of kagome metal RbV₃Sb₅ single crystals, *Chin. Phys. Lett.* **38**, 037403 (2021).
- [50] H. Luo, Q. Gao, H. Liu, Y. Gu, D. Wu, C. Yi, J. Jia, S. Wu, X. Luo, Y. Xu, L. Zhao, Q. Wang, H. Mao, G. Liu, Z. Zhu, Y. Shi, K. Jiang, J. Hu, Z. Xu, and X. J. Zhou, Electronic nature of charge density wave and electron-phonon coupling in kagome superconductor KV₃Sb₅ single crystals, *Nat. Commun.* **13**, 273 (2022).
- [51] H. Yang, Y. Zhang, Z. Huang, Z. Zhao, J. Shi, G. Qian, B. Hu, Z. Lu, H. Zhang, C. Shen, X. Lin, Z. Wang, S. J. Pennycook, H. Chen, X. Dong, W. Zhou, and H. J. Gao, Titanium doped

- kagome superconductor $\text{CsV}_{3-x}\text{Ti}_x\text{Sb}_5$ and two distinct phases, *Sci. Bull.* **67**, 2176 (2022).
- [52] See Supplemental Material at <http://link.aps.org/supplemental/10.1103/PhysRevB.111.155123> for additional measurements (band folding, polarization-dependency, momentum-independency,) and detailed simulations of spectral function with the influence of electron-mode coupling.
- [53] J. Yu, Z. Xu, K. Xiao, Y. Yuan, Q. Yin, Z. Hu, C. Gong, Y. Guo, Z. Tu, P. Tang, H. Lei, Q. K. Xue, and W. Li, Evolution of electronic structure in pristine and Rb-reconstructed surfaces of kagome metal RbV_3Sb_5 , *Nano Lett.* **22**, 918 (2022).
- [54] M. Kang, S. Fang, J. K. Kim, B. R. Ortiz, J. Yoo, B. G. Park, S. D. Wilson, J. H. Park, and R. Comin, Twofold van Hove singularity and origin of charge order in topological kagome superconductor CsV_3Sb_5 , *Nat. Phys.* **18**, 301 (2022).
- [55] Y. Hu, X. Wu, B. R. Ortiz, S. Ju, X. Han, J. Ma, N. C. Plumb, M. Radovic, R. Thomale, S. D. Wilson, A. P. Schnyder, and M. Shi, Rich nature of Van Hove singularities in kagome superconductor CsV_3Sb_5 , *Nat. Commun.* **13**, 2220 (2022).
- [56] M. Kang, S. Fang, J. Yoo, B. R. Ortiz, Y. M. Oey, J. Choi, S. H. Ryu, J. Kim, C. Jozwiak, A. Bostwick, E. Rotenberg, E. Kaxiras, J. G. Checkelsky, S. D. Wilson, J.-H. Park, and R. Comin, Charge order landscape and competition with superconductivity in kagome metals, *Nat. Mater.* **22**, 186 (2023).
- [57] Z. Jiang, H. Ma, W. Xia, Z. Liu, Q. Xiao, Z. Liu, Y. Yang, J. Ding, Z. Huang, J. Liu, Y. Qian, J. Liu, Y. Peng, S. Cho, Y. Guo, J. Liu, and D. Shen, Observation of electronic nematicity driven by the three-dimensional charge density wave in kagome lattice KV_3Sb_5 , *Nano Lett.* **23**, 5625 (2023).
- [58] M. Lindroos, S. Sahrakorpi, and A. Bansil, Matrix element effects in angle-resolved photoemission from $\text{Bi}_2\text{Sr}_2\text{CaCu}_2\text{O}_8$: Energy and polarization dependencies, final state spectrum, spectral signatures of specific transitions, and related issues, *Phys. Rev. B* **65**, 054514 (2002).
- [59] X. J. Zhou, T. Yoshida, S. A. Kellar, P. V. Bogdanov, E. D. Lu, A. Lanzara, M. Nakamura, T. Noda, T. Kakeshita, H. Eisaki, S. Uchida, A. Fujimori, Z. Hussain, Z.-X. Shen, Dual nature of the electronic structure of $(\text{La}_{2-x-y}\text{Nd}_y\text{Sr}_x)\text{CuO}_4$ and $\text{La}_{1.85}\text{Sr}_{0.15}\text{CuO}_4$, *Phys. Rev. Lett.* **86**, 5578 (2001).
- [60] Y. Wu, Y. Fang, P. Li, Z. Xiao, H. Zheng, H. Yuan, C. Cao, Y.-f. Yang, and Y. Liu, Bandwidth-control orbital-selective delocalization of $4f$ electrons in epitaxial Ce films, *Nat. Commun.* **12**, 2520 (2021).
- [61] K.-J. Xu, Q. Guo, M. Hashimoto, Z.-X. Li, S.-D. Chen, J. He, Y. He, C. Li, M. H. Berntsen, C. R. Rotundu, Y. S. Lee, T. P. Devereaux, A. Rydh, D.-H. Lu, D.-H. Lee, O. Tjernberg, Z.-X. Shen, Bogoliubov quasiparticle on the gossamer Fermi surface in electron-doped cuprates, *Nat. Phys.* **19**, 1834 (2023).
- [62] I. M. Vishik, N. Barišić, M. K. Chan, Y. Li, D. D. Xia, G. Yu, X. Zhao, W. S. Lee, W. Meevasana, T. P. Devereaux, M. Greven, and Z.-X. Shen, Angle-resolved photoemission spectroscopy study of $\text{HgBa}_2\text{CuO}_{4+\delta}$, *Phys. Rev. B* **89**, 195141 (2014).
- [63] S. Wirth and F. Steglich, Exploring heavy fermions from macroscopic to microscopic length scales, *Nat. Rev. Phys.* **1**, 16051 (2016).
- [64] H. Yan, J. M. Bok, J. He, W. Zhang, Q. Gao, X. Luo, Y. Cai, Y. Peng, J. Meng, C. Li *et al.*, Ubiquitous coexisting electron-mode couplings in high-temperature cuprate superconductors, *Proc. Natl. Acad. Sci. USA* **120**, e2219491120 (2023).
- [65] A. W. Sandvik, D. J. Scalapino, and N. E. Bickers, Effect of an electron-phonon interaction on the one-electron spectral weight of a d -wave superconductor, *Phys. Rev. B* **69**, 094523 (2004).
- [66] L. Miao, Y. Xu, W. Zhang, D. Older, S. A. Breitweiser, E. Kotta, H. He, T. Suzuki, J. D. Denlinger, R. R. Biswas, J. G. Checkelsky, W. Wu, and L. A. Wray, Observation of a topological insulator Dirac cone reshaped by non-magnetic impurity resonance, *npj Quantum Mater.* **3**, 29 (2018).
- [67] T. Yilmaz, A. Pertsova, W. Hines, E. Vescovo, K. Kaznatcheev, A. V. Balatsky, and B. Sinkovic, Gap-like feature observed in the non-magnetic topological insulators, *J. Phys.: Condens. Matter* **32**, 145503 (2020).
- [68] A. Pertsova, P. Johnson, D. P. Arovos, and A. V. Balatsky, Dirac node engineering and flat bands in doped Dirac materials, *Phys. Rev. Res.* **3**, 033001 (2021).
- [69] K. Gofron, J. C. Campuzano, A. A. Abrikosov, M. Lindroos, A. Bansil, H. Ding, D. Koelling, and B. Dabrowski, Observation of an “extended” Van Hove singularity in $\text{YBa}_2\text{Cu}_4\text{O}_8$ by ultrahigh energy resolution angle-resolved photoemission, *Phys. Rev. Lett.* **73**, 3302 (1994).
- [70] Y. Hu, S. M. L. Teicher, B. R. Ortiz, Y. Luo, S. Peng, L. Huai, J. Ma, N. C. Plumb, S. D. Wilson, J. He, and M. Shi, Topological surface states and flat bands in the kagome superconductor CsV_3Sb_5 , *Sci. Bull.* **67**, 495 (2022).
- [71] G. Liu, G. Wang, Y. Zhu, H. Zhang, G. Zhang, X. Wang, Y. Zhou, W. Zhang, H. Liu, L. Zhao, J. Meng, X. Dong, C. Chen, Z. Xu, and X. J. Zhou, Development of a vacuum ultraviolet laser based angle-resolved photoemission system with a super-high energy resolution better than 1 meV, *Rev. Sci. Instrum.* **79**, 023105 (2008).
- [72] X. J. Zhou, S. He, G. Liu, L. Zhao, L. Yu, and W. Zhang, New developments in laser-based photoemission spectroscopy and its scientific applications: A key issues review, *Rep. Prog. Phys.* **81**, 062101 (2018).
- [73] W. Kohn and L. J. Sham, Self-consistent equations including exchange and correlation effects, *Phys. Rev.* **140**, A1133 (1965).
- [74] P. E. Blöchl, Projector augmented-wave method, *Phys. Rev. B* **50**, 17953 (1994).
- [75] G. Kresse and J. Furthmüller, Efficient iterative schemes for *ab initio* total-energy calculations using a plane-wave basis set, *Phys. Rev. B* **54**, 11169 (1996).
- [76] J. P. Perdew, K. Burke, and M. Ernzerhof, Generalized gradient approximation made simple, *Phys. Rev. Lett.* **77**, 3865 (1996).
- [77] S. Grimme, J. Antony, S. Ehrlich, and H. Krieg, A consistent and accurate *ab initio* parametrization of density functional dispersion correction (DFT-D) for the 94 elements H–Pu, *J. Chem. Phys.* **132**, 154104 (2010).
- [78] V. Popescu and A. Zunger, Effective band structure of random alloys, *Phys. Rev. Lett.* **104**, 236403 (2010).
- [79] V. Popescu and A. Zunger, Extracting E versus \vec{k} effective band structure from supercell calculations on alloys and impurities, *Phys. Rev. B* **85**, 085201 (2012).
- [80] P. V. C. Medeiros, S. Stafström, and J. Björk, Effects of extrinsic and intrinsic perturbations on the electronic structure of graphene: Retaining an effective primitive cell band structure by band unfolding, *Phys. Rev. B* **89**, 041407 (2014).
- [81] P. V. C. Medeiros, S. S. Tsirkin, S. Stafström, and J. Björk, Unfolding spinor wave functions and expectation values of

- general operators: Introducing the unfolding-density operator, [Phys. Rev. B **91**, 041116 \(2015\)](#).
- [82] A. B. Migdal, Interaction between electrons and lattice vibrations in a normal metal, [Sov. Phys. JETP **34**, 996 \(1958\)](#).
- [83] B. R. Ortiz, S. M. L. Teicher, L. Kautzsch, P. M. Sarte, J. P. C. Ruff, R. Seshadri, and S. D. Wilson, Fermi surface mapping and the nature of charge density wave order in the kagome superconductor CsV₃Sb₅, [Phys. Rev. X **11**, 041030 \(2021\)](#).